Pre-existing basement thrusts influence rifting in the Taranaki Basin, New Zealand

Katherine Siuda[1], Craig Magee[1], Rebecca E. Bell[1], **Christopher A-L Jackson[1]**, Luca Collanega[1,2]

[1]Basins Research Group (BRG), Department of Earth Science and Engineering, Imperial College, London, SW7 2BP, UK

[2]Dipartmento di Geoscienze, Universitá degli Studi di Padova, Padova, 35131, Italy

Corresponding author: c.jackson@imperial.ac.uk

Abstract

Discrete structures (e.g. faults) or pervasive fabrics (e.g. foliation), which may occur in pre-rift sedimentary and/or crystalline basement rock, can control the growth and geometry of rift-related normal fault arrays. Previous studies examining how such structures/fabrics affect rift geometry typically rely only on plan-view correlations between the strike and dip of observed or, in some cases, inferred pre- and syn-kinematic structures. Three-dimensional relationships between and kinematic evolution of, pre-existing structures/fabrics and rift-related normal faults remains poorly constrained because: (i) outcrop patterns rarely expose both rift-related normal faults *and* the underlying rock units that could host pre-kinematic structures; (ii) discrete structures or pervasive fabrics are often poorly imaged in seismic reflection data; and (iii) it is difficult to quantitatively assess how pre-kinematic structures/fabrics influence normal fault nucleation and growth. Here, we use 3D seismic reflection data from the Taranaki Basin, offshore western New Zealand to study the kinematic history of a Cenozoic, rift-related, NE-SW striking normal fault array developed above a suite of N-S striking, intra-basement reflections interpreted as Palaeozoic thrusts. Only six of the 16 mapped rift-related normal faults mirror the strike of and appear physically linked to, the basement thrusts for at least 50% of their strike length; this spatial relationship would typically be inferred to reflect reactivation and upward propagation of the basement thrusts during rifting. However, fault throw analysis reveals the normal faults nucleated in the sedimentary cover ~1–2 km above the unconformity marking the top basement. We show the rift-related normal faults propagated downwards to either intersect NE-SW striking thrust segments or twisted to become aligned with the local strike of the basement structures. We propose that the presence and subtle reactivation of basement thrusts during Cenozoic extension locally reoriented the principal stress axes within the sedimentary basin, causing rift-related normal faults to deviate from their dominant NE strike. Despite having superficially similar strikes, rift-related normal faults may not simply form due to reactivation and upward propagation of basement structures.

Introduction

Models of continental rifting commonly assume the upper crust is homogeneous, with extensional faults striking broadly perpendicular to the regional extension direction (e.g. Gupta et al., 1998; Gawthorpe and Leeder, 2000). However, several field-, seismic reflection-, and modelling-based studies indicate that pre-existing heterogeneities localised within pre-rift sedimentary or crystalline rocks underlying nascent rifts can influence the distribution, scale, and kinematics of rift-related normal fault arrays (e.g. Bartholomew et al., 1993; Faccenna et al., 1995; Henza et al., 2011; Deng et al., 2017). Here, we examine how pre-existing heterogeneities within crystalline basement (i.e. meta-sedimentary, high-grade metamorphic, or igneous rocks) may affect the kinematic history of rift-related normal faults within overlying sedimentary basins. Possible intra-crystalline, basement heterogeneities include discrete faults, shear zones, changes in rock type, and igneous intrusions. These heterogeneities can act as zones of weaknesses that may reactivate during later tectonic events, promote nucleation of later faults, and/or locally modify the regional stress field (e.g. Bartholomew et al., 1993; Faccenna et al., 1995; Clemson et al., 1997; Doré et al., 1997; Morley et al., 2004; Morley, 2010; Kirkpatrick et al., 2013; Magee et al., 2014; Phillips et al., 2016; Deng et al., 2017; Phillips et al., 2017). Basement heterogeneities can thus shape the overall rift physiography, driving development of normal faults striking oblique to the regional principal stress axes. These potential impacts on fault arrays imply that fault strike cannot easily be used to infer extension direction in areas where basement heterogeneities are present (e.g. Morley et al., 2004; Reeve et al., 2014; Peace et al., 2017). Despite their importance, it is typically difficult to assess the geometric and kinematic relationships between basement heterogeneities and overlying normal faults within sedimentary basins because: (i) outcrops rarely preserve basement structures *and* overlying normal faults, or do so only at a small scale; and (ii) deeply buried basement rocks are commonly poorly imaged in seismic reflection data, meaning we typically rely on only qualitative plan-view correlations between the strike and dip of rift-related faults and inferred basement heterogeneities.

Although critical in some basins, pre-existing basement heterogeneities may not always influence the geometric and kinematic development of rift-related fault networks (Roberts and Holdsworth, 1999; Reeve et al., 2014; Phillips et al., 2016). For example, Mesozoic rift faults in the North Sea Basin truncate, rather than reactivate, basement-involved Caledonian and Variscan structures (Roberts and Holdsworth, 1999; Reeve et al., 2014). Why the geometry and kinematics of some rift-related fault arrays are affected by pre-existing basement heterogeneities whereas others are not, remains unclear. Some studies suggest the orientation of basement heterogeneities relative to the extension direction plays a key role on the likelihood of reactivation, with those heterogeneities oriented orthogonal to σ_3 most likely to reactivate (e.g. Keep and McClay, 1997; Henza et al., 2011). Other studies show the influence of pre-existing heterogeneities is scale dependant (Kirkpatrick et al., 2013; Phillips et al., 2016). For example, the strike of rift-related faults may parallel the trend of basement heterogeneities at a regional scale but cross-cut these older structures on a local scale (e.g. Kirkpatrick et al., 2013). Furthermore, large shear zones may be more likely to reactivate than smaller ones (e.g. Phillips et al., 2016). To assess if and how basement heterogeneities control fault growth and rift development, it is key to define the 3D geometry and kinematic history of both sets of structures. 3D seismic reflection data are ideal for this type of structural geology problem; they permit 3D mapping of intra-basement structures, thereby allowing us to quantitatively analyse their geometric and kinematic relationship to later, rift-related fault networks (Reeve et al., 2014; Bird et al., 2015; Phillips et al., 2016).

The Taranaki Basin, offshore New Zealand's North Island (Fig. 1) provides an ideal opportunity to quantitatively assess the influence of pre-existing basement heterogeneities on the geometric and kinematic development of rift-related normal fault networks. This basin is imaged by high-quality, 3D seismic reflection data and is penetrated by several wells that constrain the age and composition of the basin fill. In our study area, the basement is relatively shallow and the overburden is layered and not geologically complex, meaning we can directly image and quantify basement and rift-related structures. Within the basement a series of enigmatic, NW- to NNW-striking reflections or reflection 'packages' are observed;

these have previously been interpreted as either Mesozoic faults, stratigraphic boundaries, or compressional features of unknown age or origin (Hemmings-Sykes, 2012; Reilly et al., 2015). We map and quantitatively analyse these basement structures and overlying, rift-related normal fault networks in 3D to understand the geometric and kinematic relationship between the two.

Geological Setting

The Taranaki Basin is largely located offshore the western margin of New Zealand's North Island (Fig. 1). The basin is currently situated in an extensional back-arc setting, with the Hikurangi subduction zone lying to the east, where the Pacific plate is subducting beneath the Australian plate (Fig. 1) (e.g. Giba et al., 2010).

Basement Geology

The numerous basement terranes in New Zealand were accreted throughout the Palaeozoic and Mesozoic on the palaeo-Pacific margin of Gondwana, with final accretion occurring in the Early Cretaceous (Muir et al., 2000). These terranes can be broadly grouped into three 'superterranes', each with distinct tectonic histories (Fig. 1) (Landis and Coombs, 1967). The Western Province comprises Palaeozoic, meta-sedimentary rocks from the Gondwana continental margin, and is intruded by Devonian, Carboniferous, and Cretaceous granitoids (Cooper and Tulloch, 1992; Muir et al., 2000). In contrast, the Eastern Province is sub-divided into a series of Late Palaeozoic-to-Mesozoic accreted arc terranes comprising meta-sedimentary and volcanic rocks (King and Thrasher, 1996; Scott, 2013). The Western and Eastern province superterranes are typically separated by the third superterrane, i.e. the Median Batholith (Fig. 1), which comprises a complex amalgamation of contiguous, Cordilleran-style igneous plutons, including the Rotaroa Igneous Complex (e.g. Bradshaw, 1993; King and Thrasher, 1996; Mortimer et al., 1997). Where Mesozoic volcano-sedimentary arc rocks of the Eastern Province (i.e. specifically the Drumdaun Terrance) juxtapose the Western Province, the boundary is marked by a series of ductile shear zones(Scott, 2013). The study area spans the boundary between the Western Province superterrane and Median Batholith, a boundary that is exploited by the Cape Egmont Fault (Fig. 1).

Mesozoic Rifting and Cenozoic Evolution

Rift-related uplift and erosion in the Cretaceous produced a regional unconformity, which now marks the boundary between largely crystalline basement rocks and the overlying sedimentary succession (Fig. 2). Mudstone-rich, non-marine-to-marine clastic rocks dominate the syn- and post-rift sedimentary sequence, although sandstone- and carbonate-rich formations locally occur (Fig. 2) (Reilly et al., 2015; Strogen et al., 2017). Rifting initiated ~105 Ma in response to the breakup of Gondwana and opening of the Tasman Sea, with the main period of basin-forming extension, and development of N- and NE-trending half graben, occurring in the Late Cretaceous-to-earliest Eocene (~83–55 Ma; Fig. 2) (e.g. King and Thrasher, 1996; Reilly et al., 2015; Strogen et al., 2017). During the early-to-middle Eocene (~55–40 Ma), spreading in the Tasman Sea ceased and the Taranaki Basin became tectonically quiescent, with post-rift subsidence driven by lithospheric cooling, resulting in marine transgression (Fig. 2) (King and Thrasher, 1996; Strogen et al., 2017). Thermal subsidence was followed by horizontal shortening related to the onset of subduction at the Hikurangi margin (Fig. 2) (Voggenreiter, 1993; King and Thrasher, 1996). Shortening may have initiated in the late Eocene (~43–40 Ma), accelerating in the late Oligocene-to-early Miocene (~25–20 Ma), and promoting normal fault inversion (e.g. the Whitiki Fault; Fig. 2) and thrust fault nucleation (Voggenreiter, 1993; King and Thrasher, 1996; Reilly et al., 2015). A period of back-arc extension at ~12 Ma prompted the onset of normal fault development in the northern and central regions of the Taranaki Basin (Giba et al., 2010). Back-arc extension migrated southwards into the southern Taranaki Basin between 12–4 Ma in response to progressive steepening of the subducting Pacific plate (Giba et al., 2010). Between ~4–2 Ma, extension ceased in the northern Taranaki Basin but continued in the southern portion of the basin (Giba et al., 2010). To accommodate Neogene extension, new normal faults formed, and Late Cretaceous-to-earliest Eocene, rift-related normal faults were reactivated (e.g. the Cape Egmont Fault) (Reilly et al., 2015).

Dataset and Methodology

Seismic and borehole data

We use a 3D pre-stack, time-migrated, seismic reflection dataset (Maui-3D), which was collected in 1992 and covers 1500 km^2 (Fig. 3). Bin spacing is 25 m and the data image down to 5000 ms two-way time (TWT). Data are displayed with SEG normal polarity, whereby a black reflection equates to an increase in acoustic impedance. We focus on normal faults developed within the footwall of the Cape Egmont Fault, which forms the south-eastern boundary of the study area (Fig. 3A).

We used seven exploration wells to constrain the lithology and approximate age of mapped seismic horizons in the sedimentary sequence (Fig. 3A). To determine seismic velocities for the interval of interest, checkshot data were used to plot measured depth against TWT, defining a second-order polynomial best-fit line with an R^2 value of 0.997 (Fig. 3B). Seismic velocities calculated from the checkshot data, coupled with an average dominant frequency of ~50 Hz in the sedimentary sequence, suggest the limits of separability and visibility of the seismic reflection data increase downward from ~12 and 2 m to 25 m and 3 m, respectively. Only two wells penetrate basement rocks in the study area (Fig. 3A): Maui-2 intersects ~90 m of diorite, attributed to the Rotaroa Igneous Complex of the Median Batholith, and Rahi-1 intersects ~30 m of highly weathered schist and conglomerate that mark the transition from the Western Province superterrane to the overlying sedimentary sequence (Shell BP & Todd Oil Services Ltd, 1970; Shell Oil Services Ltd, 1996). Because Maui-2 likely intersects the most western limit of the Median Batholith (Shell BP & Todd Oil Services Ltd, 1970), it is probable that the majority of the study area is underlain by schist of the Western Province (Fig. 1). Given the limited vertical extent and highly weathered nature of the basement schist intersected by Rahi-1, we consider it likely its 4.08 km s^{-1} seismic velocity calculated from the checkshot data is underestimated.

Seismic interpretation

In addition to the top basement (TB), we mapped five horizons in the sedimentary sequence (H1-H5) (Fig. 2): H1 = near Top Turi Formation (near Eocene-Oligocene boundary, ~34 Ma); H2 = Intra-Manganui/Moki (Mid Miocene, ~15 Ma); H3 = Intra-Manganui Formation (Mid-Miocene, ~11 Ma); H4 = Intra-Giant Foresets Formation (Early Pliocene, ~4 Ma); and H5 = Intra-Giant Foresets Formation (Early Pliocene, ~3 Ma). Time-structure maps were generated from these horizons to illustrate the structural style at different stratigraphic levels. Major intra-basement reflections (n = 13) and normal faults (n = 16) within the sedimentary basin were mapped in plan-view using variance time-slices and cross-correlated with vertical seismic profiles.

Quantitative fault throw analysis

For blind or surface-breaking faults that grow purely through radial tip-line propagation, areas of high-throw (i.e. a proxy for displacement) commonly occur towards the centre of the fault plane, corresponding to zones of fault nucleation and therefore more slip (e.g. Watterson, 1986; Walsh and Watterson, 1987). Large faults defined by complex throw variations are typically inferred to have grown through the coalescence of initially isolated fault segments, with low-throw regions marking zones of fault linkage (e.g. Mansfield and Cartwright, 1996; Jackson and Rotevatn, 2013). However, recent discrete numerical modelling work shows that high-throw zones may develop at points where a rift-related normal fault link to underlying, reactivated faults (Deng et al., 2017). For normal faults physically linked to reactivated structures, we cannot therefore assume that high-throw zones correlate to areas of fault nucleation (Deng et al., 2017). Regardless of where throw is accrued on a fault, the overall distribution of throw and fault-related seismic-stratigraphic relationships can still be used to determine whether the studied fault: (i) was blind throughout its history or whether it broke the depositional surface (e.g. Watterson, 1986; Walsh and Watterson, 1987); (ii) grew via linkage of initially isolated segments (Mansfield and Cartwright, 1996; Deng et al., 2017); or (iii) grew continuously or episodically, with periods of quiescence alternating with periods of subsequent reactivation and slip (e.g. Baudon and Cartwright, 2008). We mapped along-strike (*T*-*x*) and down-dip (*T*-*z*) throw variations on 15 faults in our study area to determine the spatial and temporal evolution of the rift-related normal fault array (e.g. Watterson, 1986; Walsh and Watterson, 1987; Hongxing and Anderson, 2007; Baudon and Cartwright, 2008; Giba et al., 2012; Jackson and Rotevatn, 2013).

For the *T*-*x* analyses, ~20 equally spaced throw measurements were taken along the length of each normal fault; for consistency, all *T*-*x* profiles were measured along H3, where fault connectivity is greatest. Throw values were obtained from vertical seismic sections oriented orthogonal to the local fault-strike. For *T-z* analysis, we extracted values from a seismic line perpendicular to fault strike, at the position where the maximum throw was observed on the corresponding *T-x* profile; throw measurements were taken every ~100 ms TWT vertically down the fault plane and plotted against respective hanging wall depth. Stratigraphically complex channels and clinoforms made horizon correlation over fault planes difficult between H3-H4, meaning some uncertainty in throw at these depths. Where fault-parallel folding occurs, unfolded portions of the horizon were extrapolated to the fault plane to account for ductile deformation (e.g. Mansfield and Cartwright, 1996).

We used expansion index (EI) analysis to identify periods of syn-tectonic sedimentation and to thus identify periods of fault slip (Hongxing and Anderson, 2007; Jackson et al., 2017); EI is the hanging wall thickness divided by footwall thickness for each depth interval. Values >1 indicate across-fault thickening, highlighting that the fault was active and, more precisely, surface-breaking at the time of deposition (Jackson and Rotevatn, 2013).

Depth Conversion and Decompaction

We depth-converted and decompacted a seismic line (i.e. cross-line 3151) to investigate: (i) whether the dip of imaged rift-related faults changes with depth; and (ii) the dip at which faults initiated. In particular, Horizons TB and H1–H5, as well as all the mapped faults and intra-basement reflections, were depth-converted from TWT to metres using the velocities derived from the checkshot data (Fig. 3B). These depth-converted horizons were decompacted by progressively backstripping the H5-to-seabed and H1–H5 strata; this decompaction sequence reconstructs the basin structure at the end Miocene and end Eocene, respectively. For the decompaction, we used porosity and density data for the sedimentary section penetrated by the Maui-1 and -3 boreholes, and a series of fixed parameters (Supplementary Table 1).

Results

We begin this section by outlining the seismic expression, geometry, and distribution of structures identified in the basement and overlying sedimentary basin-fill, before focusing on their geometric relationship to one another. We then use throw distributions and growth strata to determine the kinematic history of rift-related structures, and to infer how basement structures may have influenced this kinematic development.

Intra-basement Seismic Character and Structure

Towards the north of the 3D survey, we observe a series of moderate-amplitude, sub-horizontal, semi-continuous reflections in the upper ~1.5 s TWT of the basement (Figs 4 and 5A). These sub-horizontal reflections are cross-cut by 13, NW-SE to NNW-SSE striking reflections (i.e. B1-B13) that dip gently-to-moderately (~20–30°) westwards (Figs 4 and 5). The W-dipping reflections locally appear to offset the sub-horizontal reflections with a reverse sense-of-motion, although the reduced imaging quality of the intra-basement facies makes correlation of reflections across these structures difficult (Figs 4 and 5A). These W-dipping intra-basement reflections are characterised by discrete, peak-trough-peak, wavetrains of varying lateral continuity (Figs 4 and 5A). Many of the W-dipping reflections are truncated at the top of the basement (Horizon TB), with some being overlain by subtle domes along Horizon TB; these domes are onlapped by the overlying sedimentary sequence (e.g. Figs 4 and 5A). The W-dipping reflections appear to converge at depth in some regions, occasionally towards a package of relatively high-amplitude, sub-horizontal reflections (e.g. Figs 4 and 5A).

Seismic Character and Structure of the Sedimentary Cover Sequence

The sedimentary cover comprises a ~3.5 km thick package of Late Cretaceous-to-Recent strata, with clinoforms occurring between horizons H3 and H4 (i.e. Giant Foresets Formation; Figs 2 and 4). Time-structure maps of the interpreted seismic horizons all display a broad dome-like morphology corresponding to the footwall of the Cape Egmont Fault (Fig. 6). In the N of the study area, strata are offset by 16 low-throw (i.e. <109 ms TWT; ~143 m), rift-related normal faults (F1-F16). These normal faults are ~4.3–14.5 km long, strike broadly NE-SW to NNE-SSW, dip westwards at ~60° (i.e. except for F4 and F16, which dip eastwards), and occasionally associated with minor antithetic normal faults (Figs 4, 5A, and 6; Supplementary Table 2). Several normal fault segments locally display NW-SE strikes (e.g. F5; Fig. 6). Normal fault connectivity is greatest between H2 and H3, with many of the normal faults tipping out downwards within the sedimentary sequence, although some extend to and terminate at Horizon TB (Figs 4, 5A, and 6). No normal faults appear to extend downward into the basement (e.g. Figs 4 and 5). In cross-section the normal faults appear planar or listric (Figs. 4, 5, and 7). Whilst depth-conversion and decompaction slightly reduces the down-dip curvature of apparently listric faults, their calculated End Miocene geometry remains non-planar (Fig. 7). In the depth-converted and decompacted section, the lower portions of some rift-related normal faults appear to curve towards and may connect to the intersection between the intra-basement reflections and Horizon TB.

Basement Structure-Normal Fault Plan-view Relationship

There is a broad spatial correlation between the location and extent of the major normal faults and that of the west-dipping, intra-basement reflections (Fig. 8). Of the 16 normal faults, 14 appear physically connected to the intra-basement structures at their lower tip for at least some of their strike length (Figs 4, 5A, and 8; Supplementary Table 2). Six normal faults (i.e. F2, F4-6, F10, and F11) are physically connected to intra-basement structures for ≥50% of their strike length (Fig. 8 and Supplementary Table 2). These connections typically occur where the basement structures locally trend N or NE, similar to the predominant strike of the overlying normal fault array (Fig. 8). However, we also observe two, entire NW-SE striking normal faults (i.e. F6 and F9) and three NW-SE striking segments of longer faults (i.e. parts of F5 and F13) that connect to basement structures (Fig. 8). Four of the 13 west-dipping, intra-basement reflections that terminate at the basement-cover interface (i.e. B4, B9, B10, and B11) are not overlain by normal faults (Fig. 8). Decompaction to the End Eocene indicates an abrupt change in dip between the normal faults (~60°) and the basement structures (20–30°) (Fig. 7).

Quantitative Fault Throw Analysis

Throw-length (T-x) profiles

We recognise two types of *T-x* plots (Fig. 9): (i) those characterised by simple bell-shaped profiles (i.e. F1, F4, F10, and F12), where maximum throw occurs roughly at the fault centre and decreases relatively smoothly towards the lateral fault tips; and (ii) those (i.e. 12 of 16) displaying a segmented profile defined by multiple throw minima. Of the 26 throw maxima identified across all *T-x* plots, 13 occur on a fault segment physically connected to an intra-basement reflection (Fig. 9).

Throw-depth (T-z) profiles

We also recognise two types of *T-z* plot (Fig. 10): (i) those (i.e. 7 of 16) displaying 'D'-shaped profiles, where maximum throw occurs in the sedimentary section between ~1.2–2.3 s TWT (i.e. ~H2–H4), decreasing gradually upwards and downwards before abruptly decreasing at the fault tips; and (ii) those (i.e. 9 of 16) characterised by 'B'-shaped profiles, in which two or more throw maxima, at variable depths, are separated by pronounced throw minima. For example, F10 displays a 'B'-shaped *T-z* profile defined by two throw maxima, located just below H1 (44 ms TWT) and between H3–H4 (50 ms TWT), separated by a throw minimum of 30 ms TWT between H1–H2. For some faults (i.e. F3, F5, F7, F10, and F13), throw decreases to negative values (down to -24 ms TWT); this is indicative of reverse displacements (Fig. 10). Where physically connected to intra-basement reflections, normal faults show little (<20 ms TWT), if any, offset of Horizon TB (e.g. Figs 4, 5A, and 10).

To investigate whether the morphology of the *T-z* plots vary depending on whether faults or fault segments are physically connected to an intra-basement reflection, we undertook a more detailed analysis of F5. F5 was selected because: (i) its southern segment displays an abrupt change in strike, from NE to NW, where it connects to B3; (ii) its middle, NE-SW striking segment tips out above Horizon TB, and is thus disconnected from an intra-basement structure; and (iii) its northern segment, which is NW-SE striking, connects to B1 (Figs 8 and 9). The southern (connected) and central (disconnected) portions of F5 display 'D'-shaped *T-z* profiles, with maximum throw of 42 ms TWT and 45 ms TWT occurring at -1862 ms TWT and -1756 ms TWT, respectively (Fig. 10). In contrast, the northern (connected) segment of F5 is defined by a B-shaped *T-z* profile containing two throw maxima of 49 ms TWT and 43 ms TWT, separated by a throw minima of 30 ms TWT; the throw maxima occur at -1560 ms TWT and -2142 ms TWT, whereas the throw minima occurs at -1719 ms TWT (Fig. 10). There thus appears to be no systematic correlation between *T-z* profile morphology and whether F5 is connected or disconnected to an intra-basement reflection (Fig. 10). Similarly, there appears to be no relationship between the type of *T-z* profiles (i.e. D- or B-shaped) displayed for other faults that are or are not connected to intra-basement reflections (Fig. 9).

Expansion Indices

Expansion indices are close to 1 for all faults (Fig. 10). However, near the upper fault tips, values tend to be >1; e.g. up to a maximum value of 1.7 for fault F13 (Fig. 10). There is a second region of relatively high values (~1.5) between -1618 and -1893 ms TWT for faults F2, F4, F6, F9, and F14 (Fig. 10). Whether these five values are anomalous is uncertain, as this region corresponds to an interval where the faults offset stratigraphically complex, clinoform bearing strata, which makes it difficult to correlate across faults (e.g. Figs 4 and 5A). Finally, a region of values <1, where stratal units in the footwall are thicker than those in the hanging wall, occurs slightly above the basement-cover interface (Fig. 10).

Interpretation and Discussion

Origin of Intra-basement Reflections

We define two types of intra-basement reflections within the Western Province superterrane (Figs 4 and 5A): (i) sub-horizontal, semi-continuous reflections, which we attribute to bedding and/or foliations within the meta-sedimentary schistose basement rock; and (ii) N-striking, gently to moderately inclined, W-dipping reflections that cross-cut and occasionally offset the sub-horizontal reflections. The peak-trough-peak wavetrain characterising the W-dipping intra-basement reflections is more complex than a single trough or peak (Figs 4 and 5A), suggesting they represent an amalgamation of reflections emanating from closely spaced interfaces (i.e. they are tuned reflection packages; Brown, 2004). Similar intra-basement reflection geometries and wavetrain configurations have been observed in the North Sea, where they have been attributed to layered mylonite zones (Reeve et al., 2014; Magee et al., 2016). We suggest the W-dipping intra-basement reflections observed here likely correspond to thrust faults, which may be marked by a layered mylonite core. Our interpretation of the W-dipping intra-basement reflections as thrust faults is based on their: (i) consistent ~20–30° dip; (ii) minor reverse offset of sub-horizontal intra-basement reflections (e.g. B3 and B7; Figs 4 and 5A); and (iii) apparent down-dip convergence and flattening towards sub-horizontal intra-basement reflections that could represent a floor thrust (Figs 4 and 5A). The inferred intra-basement thrusts are truncated at their tops by an unconformity (~95 Ma) marking the basement-cover interface, indicating thrusting occurred before the Late Cretaceous (Figs 2, 4, and 5A). We tentatively suggest thrusting occurred during the Early Cretaceous (~128–110 Ma), in conjunction with shortening and shearing related to terrane accretion along the subducting palaeo-Pacific margin of Gondwana and emplacement of Median Batholith components (Fig. 11) (Scott, 2013). Palaeogeographic reconstructions support our inference that the study area overlies a region of Early Cretaceous shortening, showing that the strike of the inferred basement thrusts was sub-parallel to the trend of the Palaeo-Pacific subduction zone (Fig. 11).

Normal Fault Evolution

Nucleation and Growth of the Normal Faults

All *T-z* plots show the same broad pattern, with a throw maxima within the sedimentary sequence that decreases downwards towards the basement and upwards towards the seabed (Fig. 10). Importantly, there is very little offset of Horizon TB, and throw maxima are not observed at the base of *T-z* profiles where normal faults connect to intra-basement thrusts (Figs 4, 5A, and 10). Furthermore, decompaction suggests there is a marked difference between the dip of the normal faults (~60°) and that of the inferred thrusts (i.e. ~20–30°), although the former at times do appear to curve towards the latter (Fig. 7). These observed throw distributions and fault geometries suggest: (i) basement thrusts did not reactivate as normal faults and propagate upwards into the sedimentary sequence during rifting (Faccenna et al., 1995); and (ii) it is unlikely zones of high-throw observed on the normal faults can be attributed to linkage to basement structures (cf. Deng et al., 2017). We consider it likely that, during NW-directed rifting (e.g. King and Thrasher, 1996; Reilly et al., 2015; Strogen et al., 2017), these broadly NW-SE striking, gentle-to-moderate dipping (i.e. 20–30°) basement thrusts were not favourably oriented with respect to the prevailing stress field, and were thus not significantly reactivated. Instead, throw distribution patterns imply the rift-related faults nucleated within the sedimentary succession and propagated both downwards and upwards. We interpret that the D-shaped *T-z* profiles represent nucleation between ~H2–H4, with growth dominated by continuous, radial tip-line propagation (Fig. 10). We consider the B-shaped profiles reflect dip linkage, via intervening throw minima and related relays, between two or more initially isolated fault segments that nucleated at various stratigraphic levels (Fig. 10). In addition to the constraints on vertical fault growth provided by the *T-z* profiles, the *T-x* plots suggest that, at the level of inspection, lateral growth of the normal faults involved either continuous, radial tip-line propagation (i.e. bell-shaped profiles) or the coalescence of initially isolated segments that linked along-strike (i.e. segmented profiles) (Fig. 9).

Although throw distributions can be used to identify *where* nucleation occurred, it is commonly difficult to assess *when* nucleation occurred; all we can infer from *T-z* and *T-x* analyses is that nucleation occurred *after* deposition of the strata hosting the throw maxima. For example, the stratigraphically lowest throw maxima we identify occur just below H1 (e.g. F10), implying all normal faults are post-Cretaceous (Figs 2 and 10). However, dip-linked faults display throw maxima at various stratigraphic levels (e.g. F10 displays throw maxima below H1 and between H3–H4; Fig. 10), which could be explained by either of the following end-members scenarios: (i) nucleation of the lower fault segment and subsequent nucleation of the upper fault segment after a period of tectonic quiescence; or (ii) synchronous nucleation of both the lower and upper faults segments after deposition of strata hosting the uppermost throw maxima. Importantly, negative throw values are observed towards the base of some dip-linked faults (i.e. F3 and F10; Fig. 10), indicating they were inverted during the Miocene shortening (Fig. 2) (Reilly et al., 2015); this suggests that at least the lower segments of F3 and F10 formed *before* Miocene inversion. We attribute this early normal fault formation to the Late Cretaceous-to-Early Eocene rifting event identified in the Taranaki Basin (e.g. Giba et al., 2010; Hemmings-Sykes, 2012; Reilly et al., 2015; Strogen et al., 2017). Our observations also imply that the upper segments of F3 and F10, which likely grew in response to dip-linkage and display throw maxima in strata between H3–H4 (Fig. 10), nucleated after inversion. This later phase of normal faulting is supported by the steep throw gradients and increase in EI >1.5 observed at the top of most *T-z* profiles, which indicate deposition of H4–H5 (6.6–2.6 Ma) strata was syn-kinematic (Fig. 10). We suggest Miocene-Pleistocene back-arc extension prompted this late-stage normal faulting (Giba et al., 2010; Reilly et al., 2015).

Influence of basement heterogeneities on normal faulting

Having established that the nucleation and growth history of the observed normal faults likely cannot be attributed to the reactivation and upward propagation of pre-existing basement heterogeneities (i.e. thrust faults), we can now assess how, if at all, the inferred basement thrusts influenced Cenozoic extension. Plan-view observations indicate the broadly NE-SW striking normal faults physically connect to subjacent basement thrusts primarily when the latter deviate from their dominant NW-SE to NNW-SSE strike to instead strike NE-SW (Fig. 8). In particular, 10 of the 14 NE-SW striking normal faults connect to NE-SW striking portions of basement thrusts for up to ~80% of their length (Fig. 8 and Supplementary Table

2); for the remaining faults, F8 and F16 strike NE-SW but do not connect to basement thrusts, F6 and F9 are NW-SE striking and connect to NW-SE striking basement thrusts, and only NW-SE striking segments of F5 and F13 connect to basement thrusts (Fig. 8). Observed connections between most of the rift-perpendicular normal faults and NE-SW striking portions of basement thrusts suggests the latter influenced fault nucleation and growth. We hypothesise that, during NW-directed rifting, the NE-SW striking segments of the intra-basement thrusts were favourably oriented relative to the regional stress field and thus accumulated stress. Whilst it does not appear that these basement thrust segments slipped significantly during rifting (i.e. they did not propagate upwards into the overlying sedimentary rocks), such a local build-up of stress may have augmented extension within sedimentary cover and thus promoted the nucleation of normal faults that, through growth, would link to the basement thrusts (e.g. Jackson and Rotevatn, 2013). In some places, accumulation of stress on NW-SE striking basement thrusts may have generated local stress fields that prompted either: (i) nucleation and growth of NW-SE striking normal faults (e.g. F6 and F9; Fig. 8); or (ii) rotation of NE-striking, downward propagating normal fault segments to assume NW strikes (e.g. F5 and F13; Fig. 8). Importantly, our results show that that rift-related faults (e.g. F8 and F16) can also form independent of apparently favourably oriented basement structures.

Conclusions

We describe a series of enigmatic, NW-SE to NNW-SSE striking, W-dipping, intra-basement seismic reflections from the meta-sedimentary Western Province superterrane located offshore western New Zealand in the Taranaki Basin. We interpret these W-dipping intra-basement reflections as thrust faults that probably developed during terrane accretion along the subducting palaeo-Pacific margin of Gondwana in the Early Cretaceous. Within the sedimentary sequence above the basement, we map 16, NE-SW striking normal faults. The spatial distribution of the intra-basement thrusts and overlying normal faults is similar, with 14 of the latter physically connecting to the former for at least part of their strike length. Fault throw analysis reveals that the normal faults nucleated within the sedimentary sequence and grew through radial tip-line propagation and/or linkage between fault segments, both along-strike and down-dip. Inversion of the normal faults in the Miocene indicates that some fault segments nucleated during Late Cretaceous-to-earliest Eocene extension, whilst a later phase of Miocene-to-Recent back-arc extension has promoted the nucleation and growth of new faults that link to pre-existing faults. Linkage between the normal faults and pre-existing basement thrusts typically occurs where the former are locally oriented NE-SW, parallel to the overall strike of the normal faults. Some normal faults also appear to bend towards NW-SE striking basement thrusts in plan-view, deviating from their predominant NE-SW strike. These observations imply that basement-hosted structures partly influenced the geometry and kinematics of later, rift-related faulting, but this control is not as significant as documented in other studies. The cause for this variability between locations is unclear, but it may reflect the fact that, in the Taranaki Basin: (i) pre-existing structures have low dips and may thus be hard to reactivate in extension; and (ii) the principal NW-SE strike of the basement thrusts were not favourably oriented during Cenozoic, NE-SW extension. We conclude that simple 2D, plan-view observations alone may not reveal the true geometric and kinematic relationships between basement and cover structures.

Acknowledgments

The work formed the MSci project of KS. CM is funded by an Imperial College Research Fellowship. We thank Midland Valley for use of the MOVE software and Schlumberger for access to Petrel. New Zealand Petroleum and Minerals are thanked for data provision; data and associated reports relevant to this study can be obtained through www.nzpam.govt.nz.

Figure captions

Figure 1: Map of the study area highlighting the distribution of the three superterranes (i.e. the Western Province, Median Batholith, and Eastern Province) and major tectonic faults, including: TF = Taranaki Fault; CEF = Cape Egmont Fault; MaF = Manaia Fault; MoF = Motumate Fault; MF = Maari Fault; and WF = Whitiki Fault. The location of the Maui-3D seismic reflection survey is also shown. Inset map shows the Taranaki Basin relative to the superterranes that comprise the basement across New Zealand. AP is the Australian Plate and PP is the Pacific Plate. Redrawn from Muir et al. (2000).

Figure 2: Tectonic and chronostratigraphic chart for the southern Taranaki Basin. Modified from King and Thrasher (1996), Kroeger et al. (2013), and Reilly et al. (2015).

Figure 3: (A) Map highlighting the 3D seismic survey and distribution of wells in the study area. (B) Time-depth plot of checkshot data for the seven wells used.

Figure 4: Uninterpreted and interpreted seismic section showing the W-dipping, intra-basement reflections and rift-related normal faults in the overlying sedimentary basin-fill. The intra-basement reflections appear to converge at depth and, in places, show minor evidence of reverse motion.

Figure 5: (A) Uninterpreted and interpreted seismic section showing the W-dipping, intra-basement reflections and rift-related normal faults in the overlying sedimentary basin-fill. (B)

Map of the intra-basement reflections (B1–B13). (C) Rose diagram plotting the average strike of each intra-basement reflection.

Figure 6: Time-structure maps for horizons TB and H1–H5. Boreholes (white circles) and rift-related fault polygons are shown; the trace of the WF is also depicted. Inset within the Horizon H2 map is a rose diagram plotting the average strike of each rift-related fault (F1–F16).

Figure 7: Depth-conversion of present day time data and decompaction to the End Miocene. See text for discussion.

Figure 8: Map showing the plan-view correlation of the intra-basement reflections and rift-related normal faults. Zones of physical linkage between rift-related normal faults and underlying intra-basement reflections are highlighted and the average strike of each zone plotted on the inset rose diagram.

Figure 9: *T*-*x* plots for F1–F16. Yellow areas correspond to portions of the faults physically linked to underlying intra-basement reflections. Each measurement is shown with a 10% error bar. See text for discussion.

Figure 10: *T*-*z* and expansion index plots for F1–F16. See Figure 9 for profile locations (red dashed lines). See text for discussion.

Figure 11: Palaeogeographic reconstruction of New Zealand ~110 Myr, showing the study rea position relative to the zone of Cretaceous shortening between the Western and Eastern Province superterranes. Modified from Scott (2013).

References

Bartholomew, I., J. Peters, and C. Powell, 1993, Regional structural evolution of the North Sea: oblique slip and the reactivation of basement lineaments: Geological Society, London, Petroleum Geology Conference series, p. 1109-1122.

Baudon, C., and J. Cartwright, 2008, The kinematics of reactivation of normal faults using high resolution throw mapping: Journal of Structural Geology, **30**, 1072-1084.

Bird, P., J. Cartwright, and T. Davies, 2015, Basement reactivation in the development of rift basins: an example of reactivated Caledonide structures in the West Orkney Basin: Journal of the Geological Society, **172**, 77-85.

Bradshaw, J., 1993, A review of the Median Tectonic Zone: terrane boundaries and terrane amalgamation near the Median Tectonic Line: New Zealand journal of geology and geophysics, **36**, 117-125.

Brown, A. R., 2004, Interpretation of three-dimensional seismic data: AAPG Memoir 42, SEG Investigations in Geophysics No. 9, v. 42: Oklahoma, USA, AAPG and SEG.

Clemson, J., J. Cartwright, and J. Booth, 1997, Structural segmentation and the influence of basement structure on the Namibian passive margin: Journal of the Geological Society, **154**, 477-482.

Cooper, R., and A. Tulloch, 1992, Early Palaeozoic terranes in New Zealand and their relationship to the Lachlan Fold Belt: Tectonophysics, **214**, 129-144.

Deng, C., R. L. Gawthorpe, E. Finch, and H. Fossen, 2017, Influence of a pre-existing basement weakness on normal fault growth during oblique extension: Insights from discrete element modeling: Journal of Structural Geology, **105**, 44-61.

Doré, A., E. Lundin, C. Fichler, and O. Olesen, 1997, Patterns of basement structure and reactivation along the NE Atlantic margin: Journal of the Geological Society, **154**, 85-92.

Faccenna, C., T. Nalpas, J.-P. Brun, P. Davy, and V. Bosi, 1995, The influence of pre-existing thrust faults on normal fault geometry in nature and in experiments: Journal of Structural Geology, **17**, 1139-1149.

Gawthorpe, R., and M. Leeder, 2000, Tectono-sedimentary evolution of active extensional basins: Basin Research, **12**, 195-218.

Giba, M., A. Nicol, and J. Walsh, 2010, Evolution of faulting and volcanism in a back-arc basin and its implications for subduction processes: Tectonics, **29**.

Giba, M., J. J. Walsh, and A. Nicol, 2012, Segmentation and growth of an obliquely reactivated normal fault: Journal of Structural Geology, **39**, 253-267.

Gupta, S., P. A. Cowie, N. H. Dawers, and J. R. Underhill, 1998, A mechanism to explain rift-basin subsidence and stratigraphic patterns through fault-array evolution: Geology, **26**, 595-598.

Hemmings-Sykes, S., 2012, The influence of faulting on hydrocarbon migration in the Kupe area, south Taranaki Basin, New Zealand: MSc Thesis thesis, University of Wellington.

Henza, A. A., M. O. Withjack, and R. W. Schlische, 2011, How do the properties of a pre-existing normal-fault population influence fault development during a subsequent phase of extension?: Journal of Structural Geology, **33**, 1312-1324.

Hongxing, G., and J. K. Anderson, 2007, Fault throw profile and kinetmatics of normal fault: Conceptual models and geologic examples: Geological Journal of China Universities, **13**, 13.

Jackson, C. A.-L., R. E. Bell, A. Rotevatn, and A. B. Tvedt, 2017, Techniques to determine the kinematics of synsedimentary normal faults and implications for fault growth models: Geological Society, London, Special Publications, **439**, SP439. 22.

Jackson, C. A. L., and A. Rotevatn, 2013, 3D seismic analysis of the structure and evolution of a salt-influenced normal fault zone: A test of competing fault growth models: Journal of Structural Geology, **54**, 215.

Keep, M., and K. McClay, 1997, Analogue modelling of multiphase rift systems: Tectonophysics, **273**, 239-270.

King, P. R., and G. P. Thrasher, 1996, Cretaceous Cenozoic geology and petroleum systems of the Taranaki Basin, New Zealand, v. 2, Institute of Geological & Nuclear Sciences.

Kirkpatrick, J., F. Bezerra, Z. Shipton, A. Do Nascimento, S. Pytharouli, R. Lunn, and A. Soden, 2013, Scale-dependent influence of pre-existing basement shear zones on rift faulting: a case study from NE Brazil: Journal of the Geological Society, **170**, 237-247.

Kroeger, K. F., R. H. Funnell, A. Nicol, M. Fohrmann, K. J. Bland, and P. R. King, 2013, 3D crustal-scale heat-flow regimes at a developing active margin (Taranaki Basin, New Zealand): Tectonophysics, **591**, 175-193.

Landis, C., and D. Coombs, 1967, Metamorphic belts and orogenesis in southern New Zealand: Tectonophysics, **4**, 501-518.

Shell BP & Todd Oil Services Ltd, 1970, Well Resume Maui-2. Ministry of Economic Development New Zealand Unpublished Petroleum Report PR541.

Shell Oil Services Ltd, 1996, Rahi-1 Well Completion Report. PML381012. Ministry of Economic Development New Zealand Unpublished Petroleum Report PR2277.

Magee, C., O. B. Duffy, K. Purnell, R. E. Bell, C. A. L. Jackson, and M. T. Reeve, 2016, Fault-controlled fluid flow inferred from hydrothermal vents imaged in 3D seismic reflection data, offshore NW Australia: Basin Research, **28**, 19.

Magee, C., K. G. McDermott, C. T. Stevenson, and C. A.-L. Jackson, 2014, Influence of crystallised igneous intrusions on fault nucleation and reactivation during continental extension: Journal of Structural Geology, **62**, 183-193.

Mansfield, C. S., and J. A. Cartwright, 1996, High resolution fault displacement mapping from three-dimensional seismic data: evidence for dip linkage during fault growth: Journal of Structural Geology, **18**, 14.

Morley, C., 2010, Stress re-orientation along zones of weak fabrics in rifts: An explanation for pure extension in ‘oblique’rift segments?: Earth and Planetary Science Letters, **297**, 667-673.

Morley, C., C. Haranya, W. Phoosongsee, S. Pongwapee, A. Kornsawan, and N. Wonganan, 2004, Activation of rift oblique and rift parallel pre-existing fabrics during extension and their effect on deformation style: examples from the rifts of Thailand: Journal of Structural Geology, **26**, 1803-1829.

Mortimer, N., A. Tulloch, and T. Ireland, 1997, Basement geology of Taranaki and Wanganui Basins, New Zealand: New Zealand Journal of Geology and Geophysics, **40**, 223-236.

Muir, R., J. Bradshaw, S. Weaver, and M. Laird, 2000, The influence of basement structure on the evolution of the Taranaki Basin, New Zealand: Journal of the Geological Society, **157**, 1179-1185.

Peace, A., K. McCaffrey, J. Imber, J. Hunen, R. Hobbs, and R. Wilson, 2017, The role of pre-existing structures during rifting, continental breakup and transform system development, offshore West Greenland: Basin Research.

Phillips, T. B., C. A. Jackson, R. E. Bell, O. B. Duffy, and H. Fossen, 2016, Reactivation of intrabasement structures during rifting: A case study from offshore southern Norway: Journal of Structural Geology, **91**, 54-73.

Phillips, T. B., C. Magee, C. A.-L. Jackson, and R. E. Bell, 2017, Determining the three-dimensional geometry of a dike swarm and its impact on later rift geometry using seismic reflection data: Geology.

Reeve, M. T., R. E. Bell, and C. A. L. Jackson, 2014, Origin and significance of intra-basement seismic reflections offshore western Norway: Journal of the Geological Society [London], **171**, 1-4.

Reilly, C., A. Nicol, J. J. Walsh, and H. Seebeck, 2015, Evolution of faulting and plate boundary deformation in the Southern Taranaki Basin, New Zealand: Tectonophysics, **651**, 1-18.

Roberts, A. M., and R. E. Holdsworth, 1999, Linking onshore and offshore structures: Mesozoic extension in the Scottish Highlands: Journal of the Geological Society, **156**, 1061-1064.

Scott, J., 2013, A review of the location and significance of the boundary between the Western Province and Eastern Province, New Zealand: New Zealand Journal of Geology and Geophysics, **56**, 276-293.

Strogen, D. P., H. Seebeck, A. Nicol, and P. R. King, 2017, Two-phase Cretaceous–Paleocene rifting in the Taranaki Basin region, New Zealand; implications for Gondwana break-up: Journal of the Geological Society, **174**, 929-946.

Voggenreiter, W. R., 1993, Structure and evolution of the Kapuni Anticline, Taranaki Basin, New Zealand: Evidence from the Kapuni 3D seismic survey: New Zealand Journal of Geology and Geophysics, **36**, 77-94.

Walsh, J., and J. Watterson, 1987, Distributions of cumulative displacement and seismic slip on a single normal fault surface: Journal of Structural Geology, **9**, 1039-1046.

Watterson, J., 1986, Fault dimensions, displacements and growth: Pure and Applied Geophysics, **124**, 365-373.

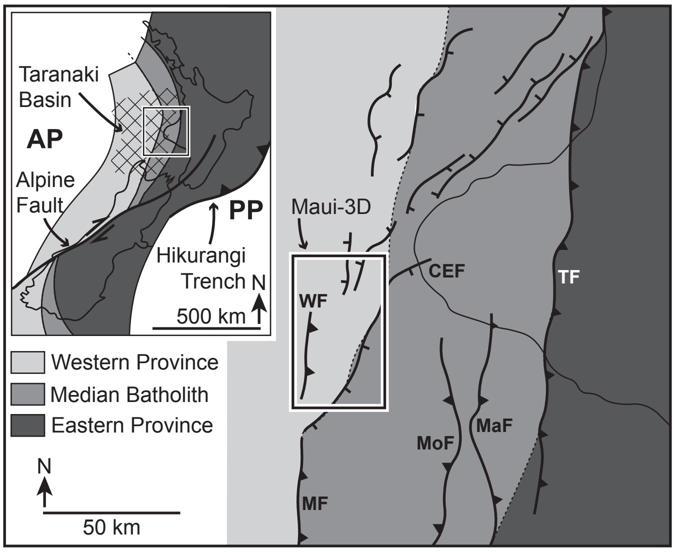

Taranaki
Basin
AP
Alpine
Fault
PP
Hikurangi
Trench
N
500 km
Western Province
Median Batholith
Eastern Province
N
50 km
Maui-3D
WF
CEF
TF
MoF
MaF
MF

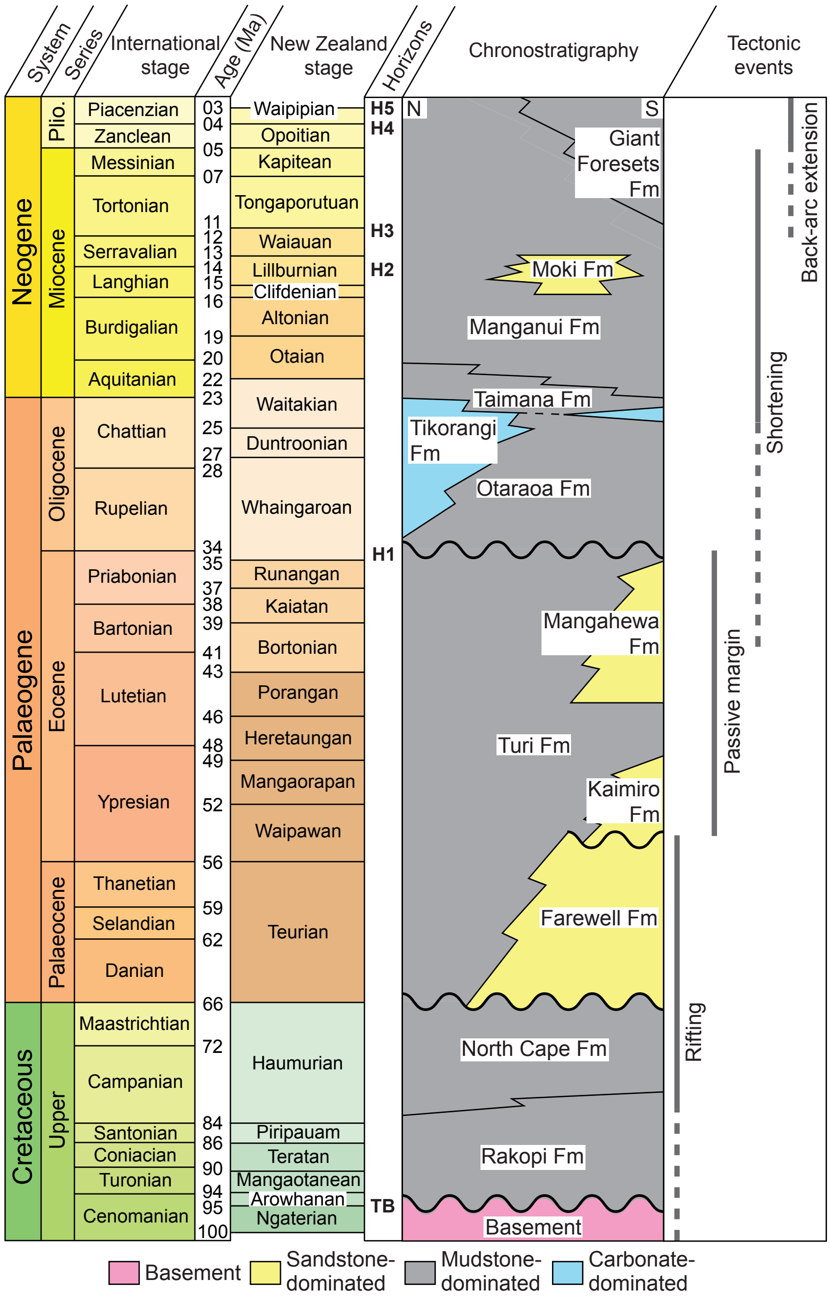
System
Series
International stage
Age (Ma)
New Zealand stage
Horizons
Chronostratigraphy
Tectonic events
Neogene
Palaeogene
Cretaceous
Plio.
Miocene
Oligocene
Eocene
Palaeocene
Upper
Piacenzian
Zanclean
Messinian
Tortonian
Serravalian
Langhian
Burdigalian
Aquitanian
Chattian
Rupelian
Priabonian
Bartonian
Lutetian
Ypresian
Thanetian
Selandian
Danian
Maastrichtian
Campanian
Santonian
Coniacian
Turonian
Cenomanian
03
04
05
07
11
12
13
14
15
16
19
20
22
23
25
27
28
34
35
37
38
39
41
43
46
48
49
52
56
59
62
66
72
84
86
90
94
95
100
Waipipian
Opoitian
Kapitean
Tongaporutuan
Waiauan
Lillburnian
Clifdenian
Altonian
Otaian
Waitakian
Duntroonian
Whaingaroan
Runangan
Kaiatan
Bortonian
Porangan
Heretaungan
Mangaorapan
Waipawan
Teurian
Haumurian
Piripauam
Teratan
Mangaotanean
Arowhanan
Ngaterian
H5
H4
H3
H2
H1
TB
N
S
Giant Foresets Fm
Moki Fm
Manganui Fm
Taimana Fm
Tikorangi Fm
Otaraoa Fm
Mangahewa Fm
Turi Fm
Kaimiro Fm
Farewell Fm
North Cape Fm
Rakopi Fm
Basement
Back-arc extension
Shortening
Passive margin
Rifting
Basement
Sandstone-dominated
Mudstone-dominated
Carbonate-dominated

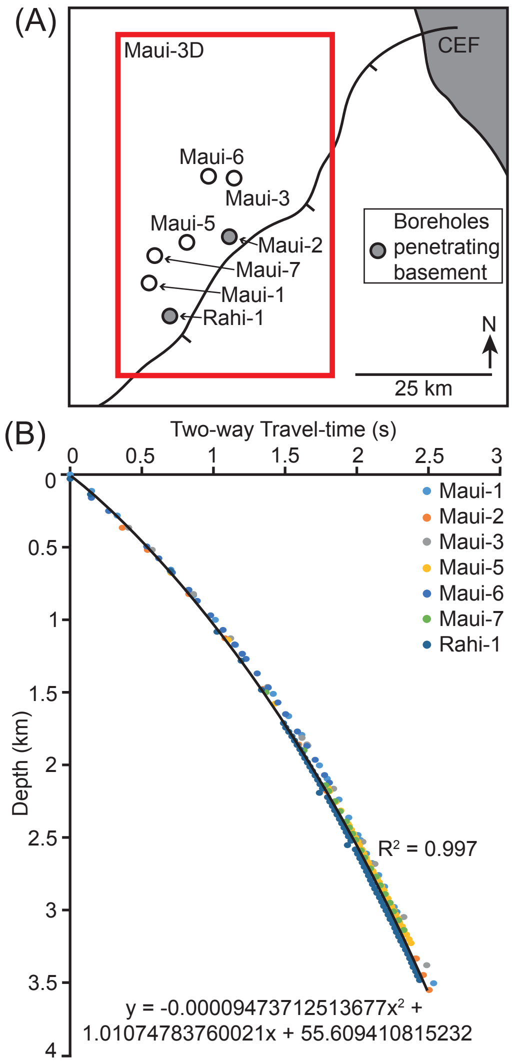
(A)
Maui-3D
CEF
Maui-6
Maui-3
Maui-5
Maui-2
Maui-7
Maui-1
Rahi-1
Boreholes penetrating basement
N
25 km
(B)
Two-way Travel-time (s)
0
0.5
1
1.5
2
2.5
3
Depth (km)
0
0.5
1
1.5
2
2.5
3
3.5
4
Maui-1
Maui-2
Maui-3
Maui-5
Maui-6
Maui-7
Rahi-1
R^2 = 0.997
y = -0.0000947371251367 7x^2 +
1.01074783760021x + 55.609410815232

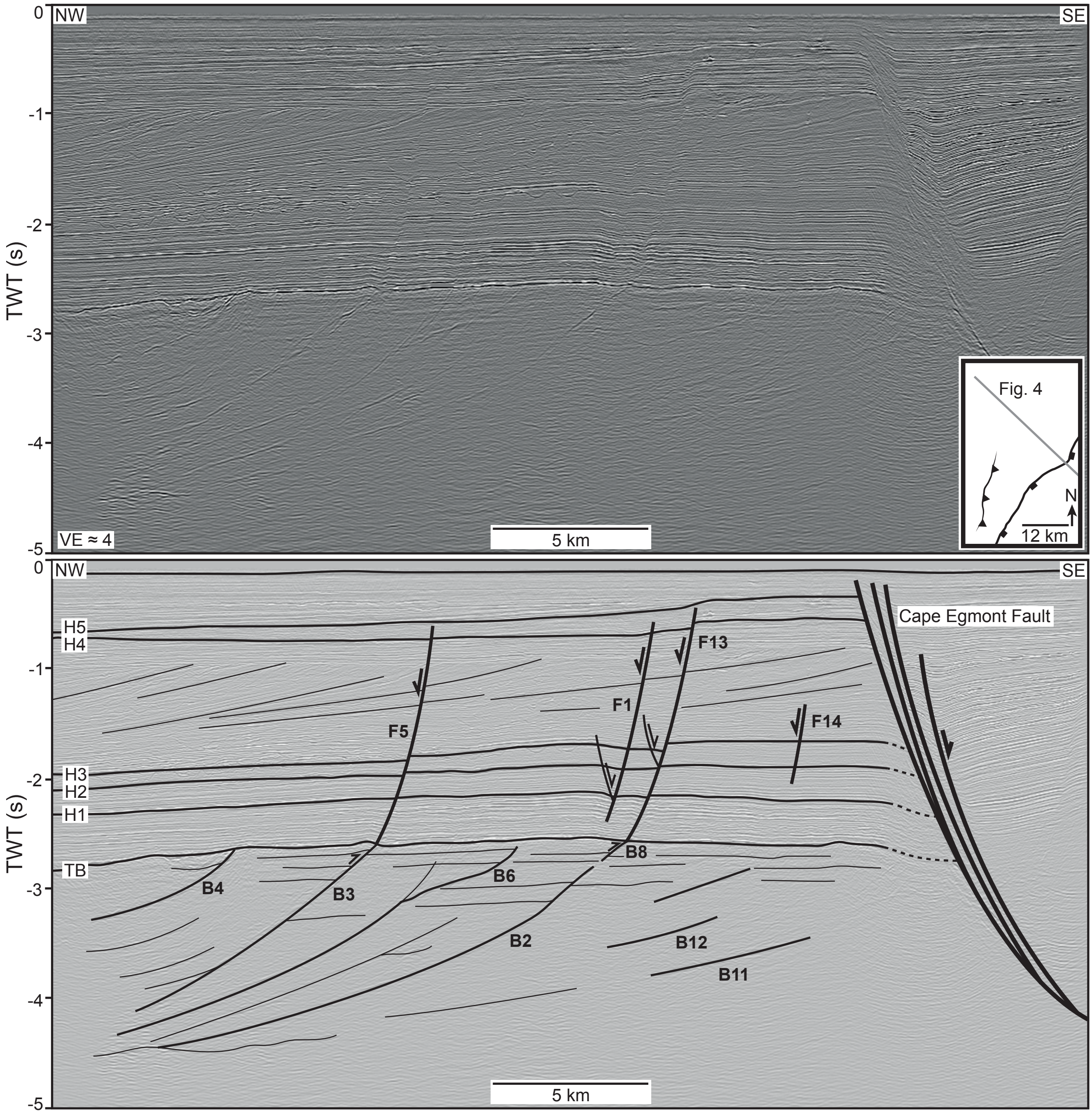

NW
SE
TWT (s)
0
-1
-2
-3
-4
-5
Fig. 4
N
12 km
VE ≈ 4
5 km
Cape Egmont Fault
H5
H4
H3
H2
H1
TB
F5
F1
F13
F14
B4
B3
B6
B8
B2
B12
B11

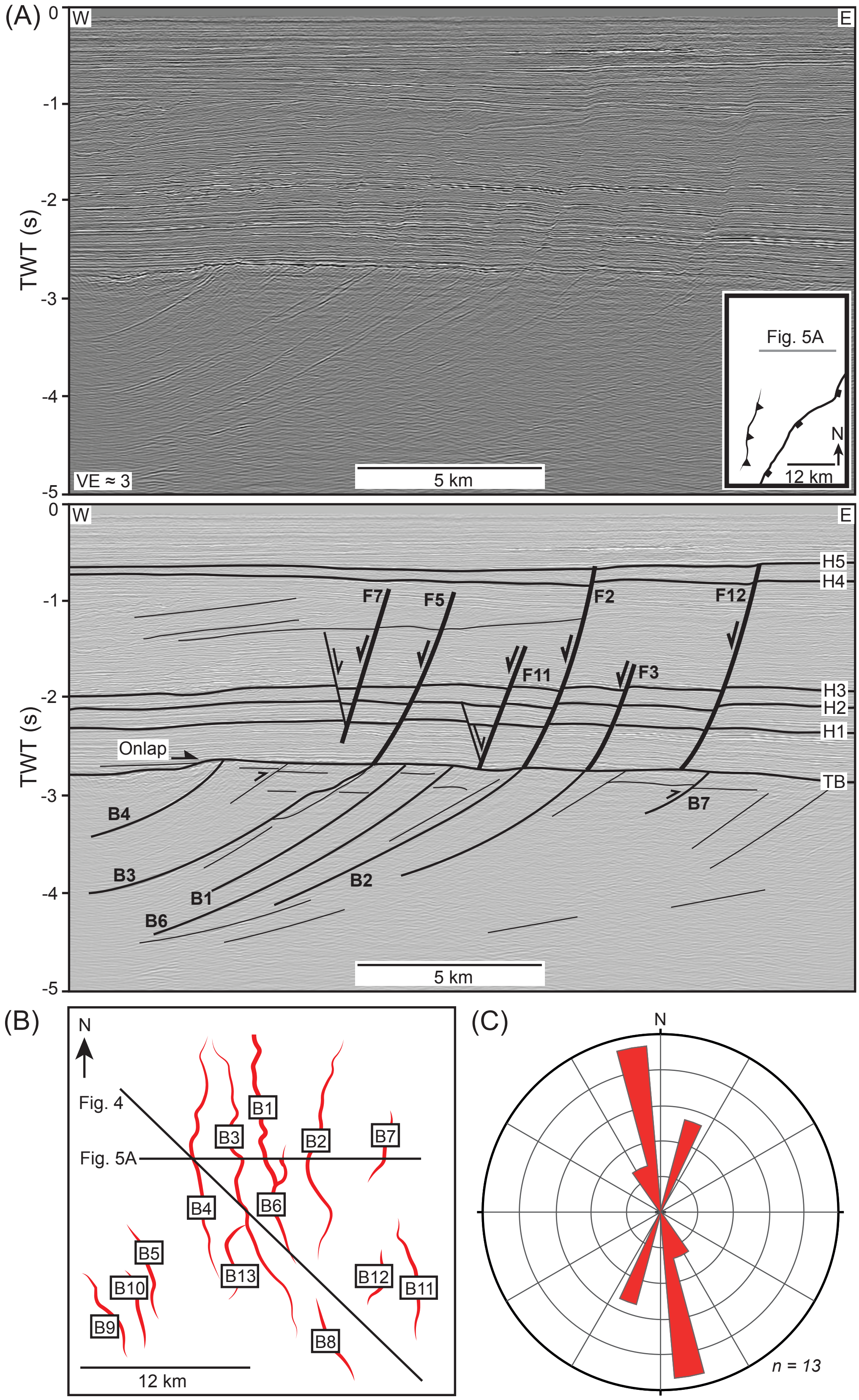

(A)
W
E
TWT (s)
0
-1
-2
-3
-4
-5
VE ≈ 3
5 km
Fig. 5A
N
12 km
H5
H4
F7
F5
F2
F12
F11
F3
H3
H2
H1
Onlap
TB
B4
B7
B3
B1
B2
B6
(B)
N
Fig. 4
Fig. 5A
B1
B2
B3
B4
B5
B6
B7
B8
B9
B10
B11
B12
B13
12 km
(C)
N
n = 13

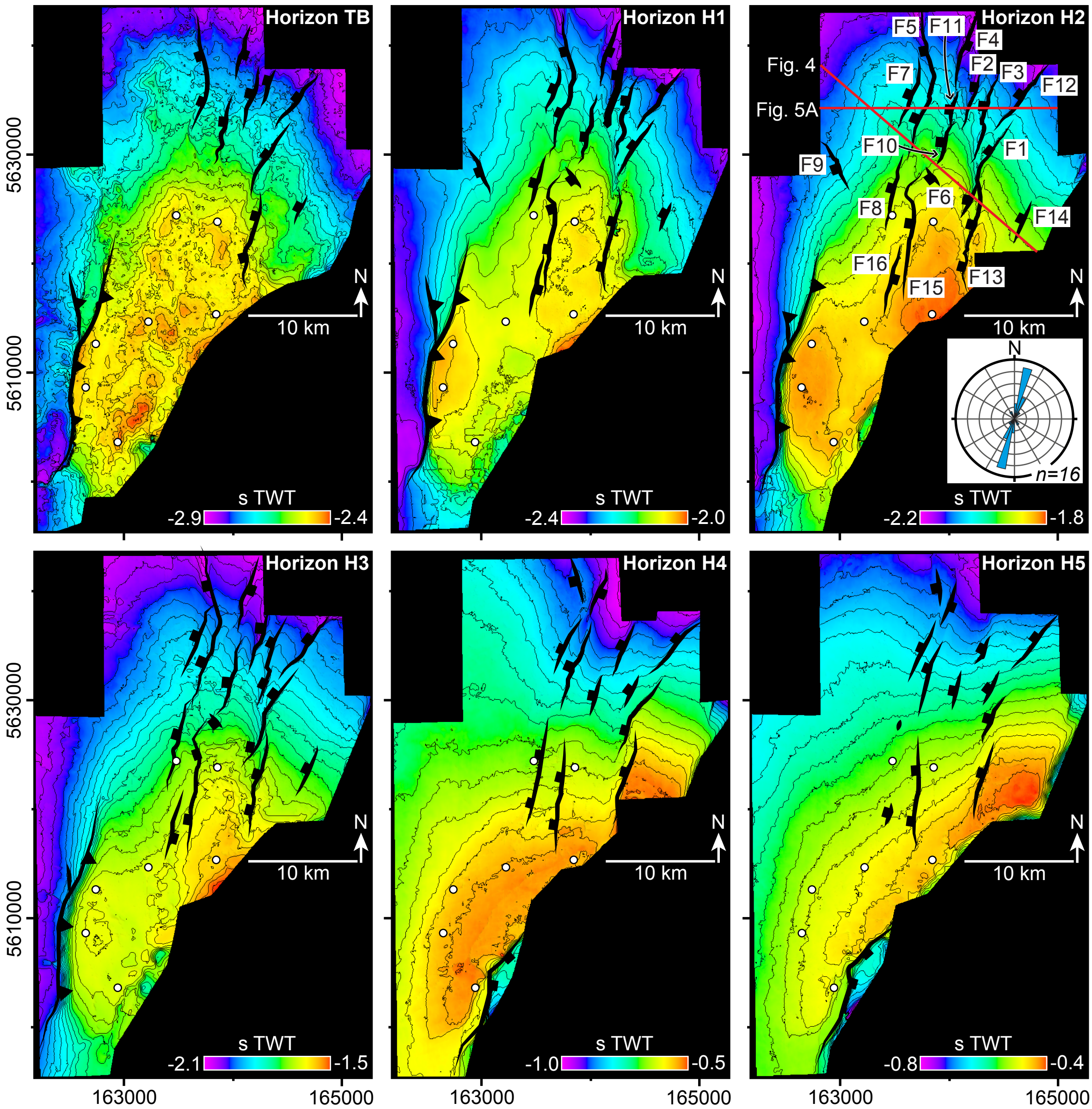

Horizon TB
Horizon H1
Horizon H2
Horizon H3
Horizon H4
Horizon H5
5630000
5610000
163000
165000
10 km
N
s TWT
-2.9
-2.4
-2.4
-2.0
-2.2
-1.8
-2.1
-1.5
-1.0
-0.5
-0.8
-0.4
Fig. 4
Fig. 5A
F1
F2
F3
F4
F5
F6
F7
F8
F9
F10
F11
F12
F13
F14
F15
F16
n=16

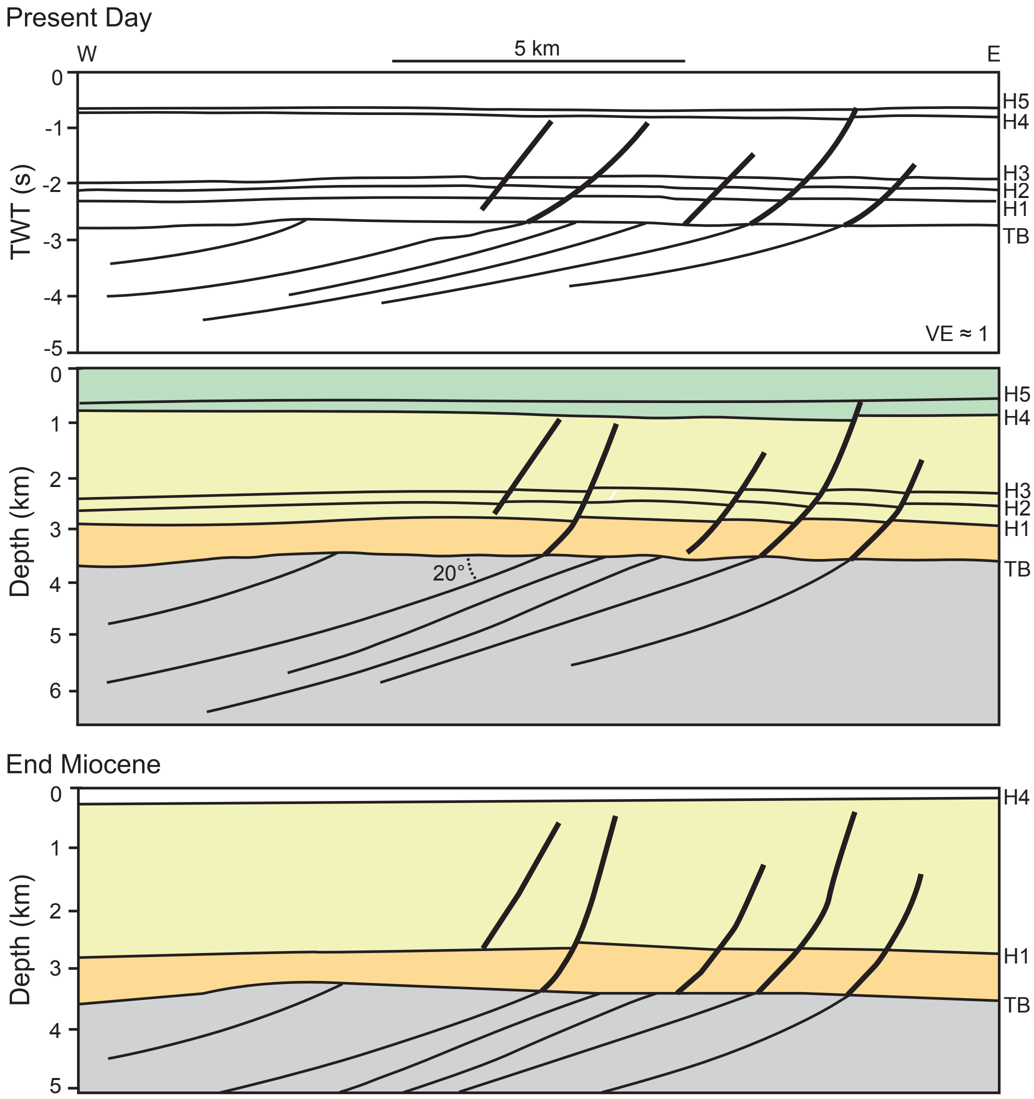
Present Day
W
5 km
E
TWT (s)
0
-1
-2
-3
-4
-5
H5
H4
H3
H2
H1
TB
VE ≈ 1
Depth (km)
20°
End Miocene

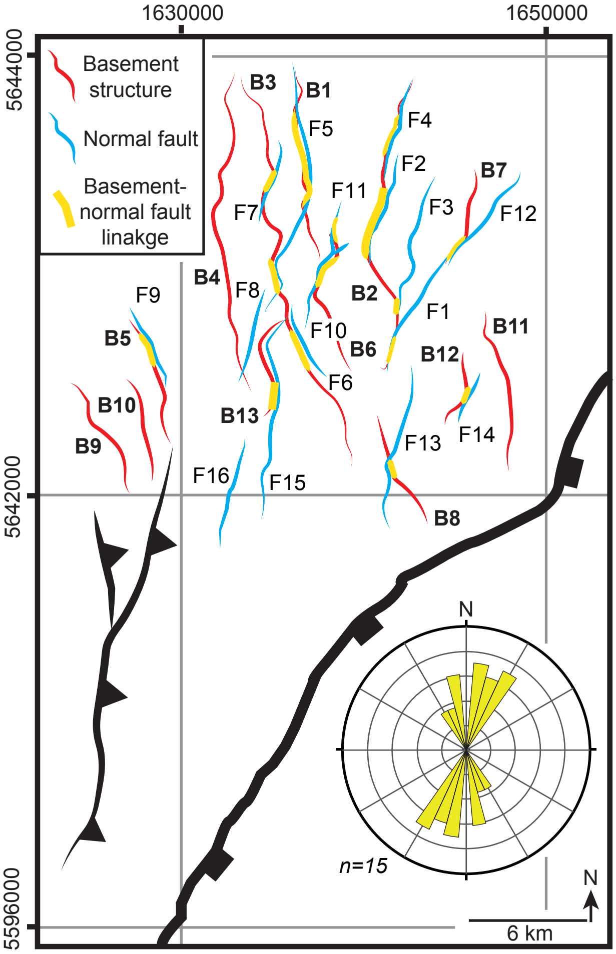

1630000
1650000
5644000
5642000
5596000
Basement structure
Normal fault
Basement-normal fault linakge
B1
B2
B3
B4
B5
B6
B7
B8
B9
B10
B11
B12
B13
F1
F2
F3
F4
F5
F6
F7
F8
F9
F10
F11
F12
F13
F14
F15
F16
N
n=15
N
6 km

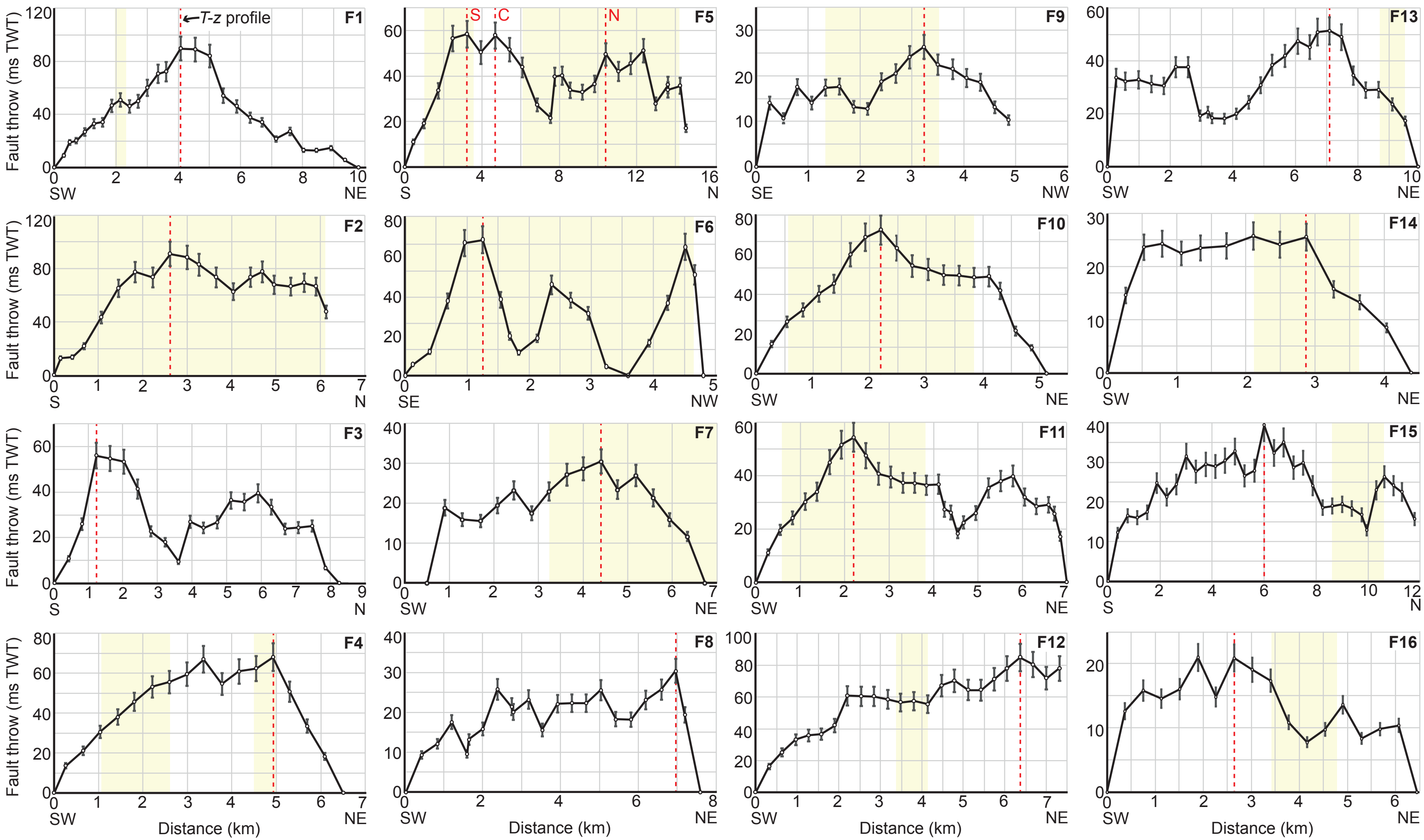

F1
←T-z profile
F5
S
C
N
F9
F13
F2
F6
F10
F14
F3
F7
F11
F15
F4
F8
F12
F16
Fault throw (ms TWT)
Distance (km)
SW
NE
S
N
SE
NW

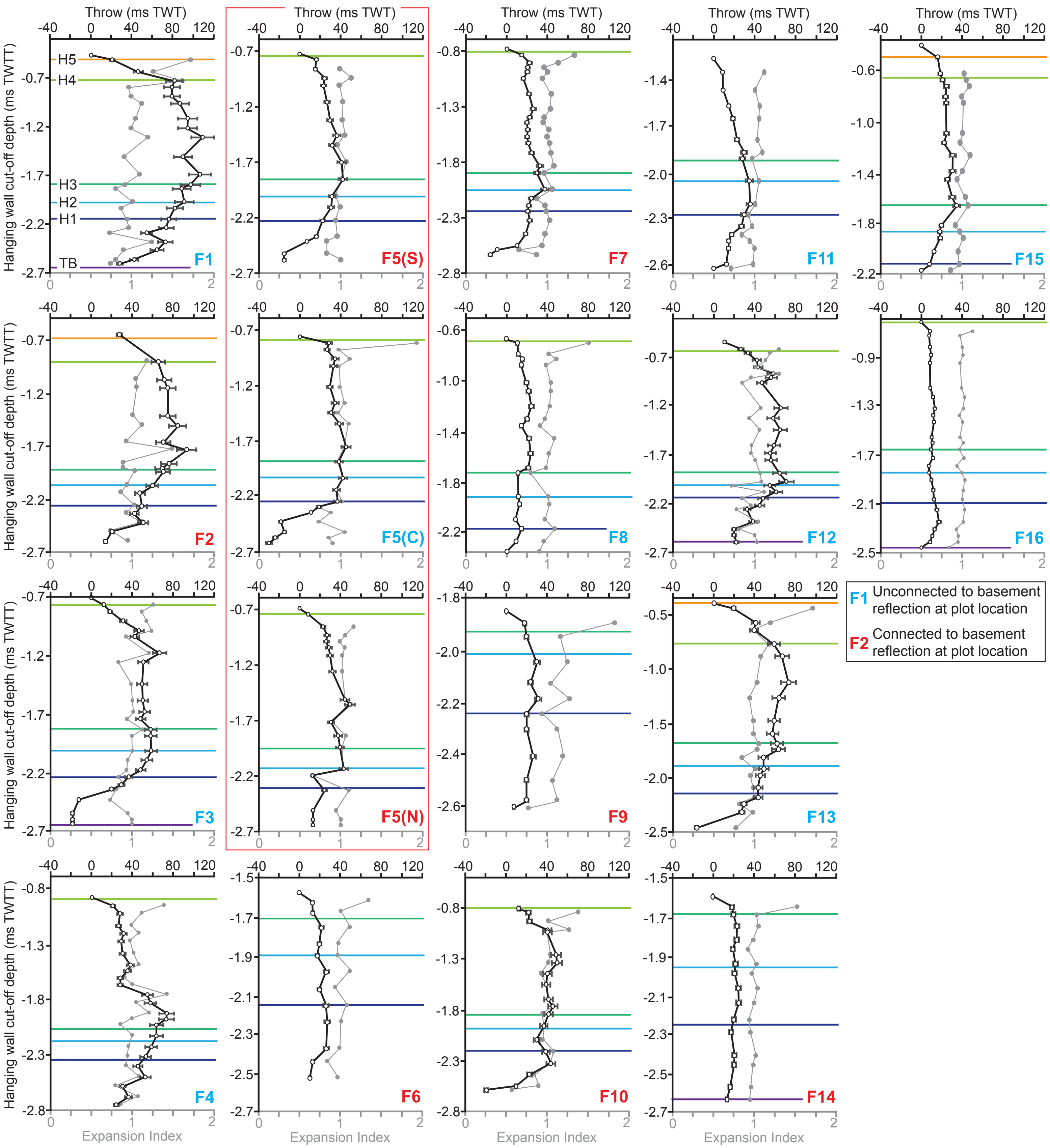

Throw (ms TWT)
Hanging wall cut-off depth (ms TWTT)
Expansion Index
H5
H4
H3
H2
H1
TB
F1
F5(S)
F7
F11
F15
F2
F5(C)
F8
F12
F16
F3
F5(N)
F9
F13
F4
F6
F10
F14
F1 Unconnected to basement reflection at plot location
F2 Connected to basement reflection at plot location

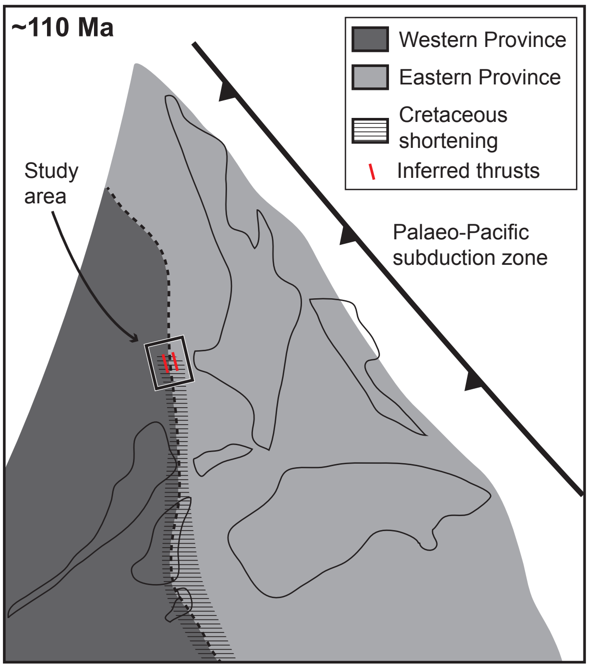
~110 Ma
Western Province
Eastern Province
Cretaceous shortening
Inferred thrusts
Study area
Palaeo-Pacific subduction zone

Supplementary Table 1: Decompaction Parameters

Obtained from Maui-1 and Maui-3 boreholes			
Unit	*Porosity*	*Density (kg m^3)*	*Lithology*
Pleistocene-to-Recent	0.22	2.2	Sandy-shale
Miocene	0.13	2.3	Sandy-shale
Palaeocene-to-Eocene	0.11	2.4	Sandy-shale

Fixed parameters	
Depth coefficient	0.39
v0 (km s) (velocity)	2.2
K (at-surface porosity)	0.5
Grainsize (mm)	0.21
Youngs modulus	23500
Poisson ratio	0.3
Isostatic method	Airy Isostasy
Compaction curve	Sclater-Christie (1980)

References

Sclater, J. G., and P. A. Christie, 1980. Continental stretching: An explanation of the post-Mid-Cretaceous subsidence of the central North Sea Basin: Journal of Geophysical Research: Solid Earth, **85**(B7), 3711-3739.

Supplementary Table 2: Rift-related fault parameters

Name	Length	Strike	Dip direction	Maximum throw	Connection to intra-basement reflection	Length of intra-basement reflection connection	Proportion of rift-related fault length in contact with intra-basement reflection
	(km)	(°)	(°)	(ms TWT)		(km)	(%)
C1	09.79	044.3	314.3	109.3	B2	2.11	021.5
C2	06.14	015.4	285.4	093.7	B2	6.14	100.0
C3	08.22	015.9	285.9	067.0	B2	0.80	009.7
C4	06.50	017.5	107.5	073.6	B2	5.51	084.7
C5	14.54	004.7	274.7	049.2	B1	8.90	088.0
					B3	3.90	
C6	04.81	324.5	234.5	027.1	B3	3.92	081.4
C7	06.24	020.0	290.0	037.0	B3	2.73	043.7
C8	07.57	016.1	286.1	024.4	N/A	N/A	N/A
C9	04.87	333.9	243.9	030.7	B5	2.04	041.9
C10	05.12	023.8	293.8	050.3	B6	2.74	053.5
C11	07.00	011.5	281.5	054.3	B6	3.99	057.0
C12	07.32	037.3	307.3	084.8	B7	1.88	025.7
C13	09.92	017.0	287.0	072.5	B3	0.88	020.2
					B8	1.13	
C14	04.39	025.0	295.0	025.4	B12	1.35	030.8
C15	12.26	006.8	276.8	034.5	B13	4.40	035.9
C16	06.44	013.3	103.3	021.0	N/A	N/A	N/A